

Review

Room Temperature Terahertz and Frequency Combs Based on Intersubband Quantum Cascade Laser Diodes: History and Future

Manijeh Razeghi ^{1,*}  and Quanyong Lu ^{1,2,*}

¹ Center for Quantum Devices, Department of Electrical Engineering and Computer Science, Northwestern University, Evanston, IL 60208, USA

² Division of Quantum Materials and Devices, Beijing Academy of Quantum Information Sciences, Beijing 100193, China

* Correspondence: razeghi@northwestern.edu (M.R.); luqy@baqis.ac.cn (Q.L.)

Abstract: The year 2024 marks the 30-year anniversary of the quantum cascade laser (QCL), which is becoming the leading laser source in the mid-infrared (mid-IR) range. Since the first demonstration, QCL has undergone tremendous development in terms of the output power, wall plug efficiency, spectral coverage, wavelength tunability, and beam quality. Owing to its unique intersubband transition and fast gain features, QCL possesses strong nonlinearities that makes it an ideal platform for nonlinear photonics like terahertz (THz) difference frequency generation and direct frequency comb generation via four-wave mixing when group velocity dispersion is engineered. The feature of broadband, high-power, and low-phase noise of QCL combs is revolutionizing mid-IR spectroscopy and sensing by offering a new tool measuring multi-channel molecules simultaneously in the μs time scale. While THz QCL difference frequency generation is becoming the only semiconductor light source covering 1–5 THz at room temperature. In this paper, we will introduce the latest research from the Center for Quantum Devices at Northwestern University and briefly discuss the history of QCL, recent progress, and future perspective of QCL research, especially for QCL frequency combs, room temperature THz QCL difference frequency generation, and major challenges facing QCL in the future.



Received: 8 December 2024

Revised: 8 January 2025

Accepted: 13 January 2025

Published: 17 January 2025

Citation: Razeghi, M.; Lu, Q. Room Temperature Terahertz and Frequency Combs Based on Intersubband Quantum Cascade Laser Diodes: History and Future. *Photonics* **2025**, *12*, 79. <https://doi.org/10.3390/photronics12010079>

Copyright: © 2025 by the authors. Licensee MDPI, Basel, Switzerland. This article is an open access article distributed under the terms and conditions of the Creative Commons Attribution (CC BY) license (<https://creativecommons.org/licenses/by/4.0/>).

Keywords: quantum cascade laser; terahertz source; frequency comb; MOCVD; inter-subband semiconductor lasers

1. Introduction

In the 1970s, the discovery of semiconductor superlattices and quantum wells [1] opened up a new direction of semiconductor bandgap engineering to be used in the research of low-dimensional quantum structures and devices. Energy bandgap engineering is also called wave function engineering or quantum tailoring engineering. Its physical connotation refers to the design and preparation of low-dimensional quantum materials and devices with designed energy bandgap characteristics and quantum confinement effects, such as semiconductor quantum super lattices, wells, wires, dots, and other optoelectronic quantum structures, by using Molecular Beam Epitaxy (MBE) or Metal Organic Chemical Vapor Deposition (MOCVD) [2,3]. For decades, band engineering technology has been widely used in the study of low-dimensional quantum systems and quantum devices. One example is the invention of quantum cascade lasers (QCLs). After the initial proposal of intersubband transitions between energy levels inside superlattice quantum wells [4], it

took more than twenty years for the first laser based on intersubband optical transition to be demonstrated [5], benefitting from significant technological advances in epitaxy and bandgap engineering [6]. The emission wavelength of QCL, which is defined by energy gaps at the quantum level rather than the bandgap of the materials, can be easily tuned by changing only the quantum well thicknesses without changing the material composition.

The QCL research was accelerated after the first demonstration of high-performance QCL using a gas source MBE at the Center for Quantum Devices at Northwestern University (CQD/NU) in 1997 [7]. After three decades of development, QCL has become the most important coherent light source in the mid-infrared (mid-IR) and terahertz (THz) ranges [8–10]. Figure 1a shows that the selected milestones of QCL research mainly focused on InP-based QCLs developed in CQD/NU. Many other application technologies, like gas sensing, spectroscopies, medical imaging, and free-space communications, are benefitting from the rapid advancement of QCL technologies [11].

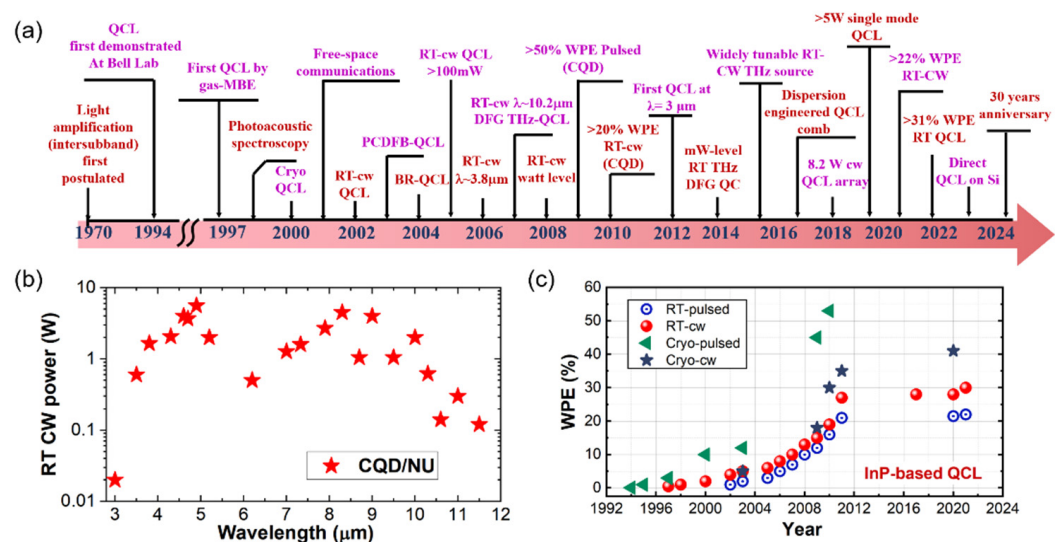


Figure 1. (a) Selected milestones of InP-based QCL research mainly achieved by CQD/NU. (b) Maximum RT-cw power of mid-IR InP-based QCLs at different wavelengths from CQD/NU. (c) Chronological map of the maximum wall plug efficiencies of RT-pulsed, RT-cw, Cryo-pulsed, and Cryo-cw operating InP-based QCLs.

High performance in power, efficiency, and spectral coverage are of fundamental importance to the above QCL applications and have been the focus of QCL research in the past years [12–15]. Figure 1b shows the maximum room temperature continuous wave (RT-cw) power of mid-IR InP-based QCLs at different wavelengths from CQD/NU, which now is the leading organization in high-power efficiency QCL research. Constant improvements in the structure design, material quality, and fabrication technologies, as well as the nonlinear effects for THz and frequency comb, have been achieved. The chronological map in Figure 1c shows the maximum wall plug efficiencies of RT-pulsed, RT-cw, Cryo-pulsed, and Cryo-cw operating InP-based QCLs. Here, cw represents continuous wave, and Cryo represents cryogenic conditions, liquid helium, or liquid nitrogen cooling. Up to now, CQD/NU is still the only research institution that is able to deliver high wall plug efficiency (WPE) above 20% at room temperature continuous wave operation.

Previously, we have demonstrated high-power RT-cw operation QCLs across a wide wavelength range from 3.0 μ m [16] to 145.6 μ m [17] and the highest RT-cw WPE of 21% at 4.9 μ m [18] and the highest RT-cw power of 8.2 W at 8.1 μ m [19]. Recently, our work on the THz difference frequency generation (DFG) QCL in 2011 demonstrated the first single-mode THz operation at room temperature and the first QCL frequency comb at

9.0 μm in 2015. In this paper, we report our recent breakthroughs in THz DFG QCLs and frequency combs, discussed in detail in the following sections: room temperature mid-IR and THz frequency combs in Section 2, THz sources based on DFG-QCL in Section 3, their future research directions in Section 4, and the conclusion perspectives in Section 5. The recently demonstrated Si-based QCLs hold great promise for next-generation THz DFG QCL and comb sources.

The principle of wavelength conversion is based on the nonlinear polarization of a dielectric medium. In a QCL medium, such nonlinear properties are strong and highly engineerable due to the strong coupling between the quantum subbands. Figure 2 depicts a QCL band structure featuring strong intersubband nonlinear processes. Among these, DFG for THz wave generation and four-wave mixing for direct frequency comb generation are currently being extensively investigated. The total polarization induced by the nonlinear processes can be expressed as [20–22]:

$$\vec{P}(t) = \chi^{(1)}\vec{E}(t) + \chi^{(2)}\vec{E}(t)\vec{E}(t) + \chi^{(3)}\vec{E}(t)\vec{E}(t)\vec{E}(t) + \dots \quad (1)$$

$$\chi^{(2)}(\omega = \omega_1 - \omega_2) = \frac{e^3}{\hbar^2 \epsilon_0} \frac{z_{12}z_{23}z_{31}}{\omega - \omega_{21} + i\Gamma_{21}} \left(\frac{N_3 - N_1}{\omega_1 - \omega_{31} + i\Gamma_{31}} + \frac{N_3 - N_2}{\omega_2 - \omega_{32} + i\Gamma_{32}} \right) \quad (2)$$

$$\chi^{(3)}(\omega_{1,4} = 2\omega_{1,1} - \omega_{1,2}) = \frac{2\delta N_0 (e \cdot z_{ij})^4}{3\hbar^3 \epsilon_0} \frac{(\delta\omega - \Delta - i/T_2)(\delta\omega - \Delta + 2i/T_2)(\Delta + i/T_2)^{-1}}{(\delta\omega - \Delta + i/T_2)(\delta\omega - \Delta - i/T_2)(\delta\omega + \Delta - i/T_2)} \quad (3)$$

where $E(t)$ is the electrical field, $\chi^{(2)}$ and $\chi^{(3)}$ are the second-order and third-order nonlinear susceptibilities originating from the strong intersubband couplings and are responsible for THz DFG and frequency comb generation, ez_{ij} is the dipole matrix element, N_i is the population density, Γ_{ij} is transition broadening, δN_0 is the volume population inversion per QC period, $\delta\omega$ is the frequency splitting, $\Delta = \omega_1 - \omega_{12}$ is frequency detuning, and T_2 is the electron dephasing time. Clearly, by optimizing $\chi^{(2)}$ and $\chi^{(3)}$, efficient THz DFG and frequency comb can be generated from QCL cavities.

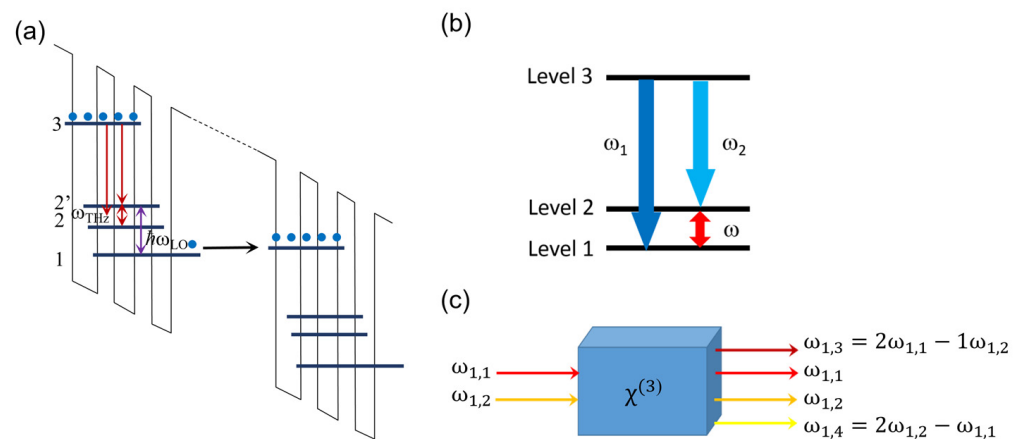


Figure 2. (a) Schematic band structure of a QCL featuring strong intersubband nonlinear processes. (b) Schematic of a difference frequency generation process in QCL. (c) Schematic of a four-wave mixing process in QCL.

2. Mid-IR to THz QCL Frequency Combs

Frequency combs, spectra of phase-coherent equidistant lines, have revolutionized time and frequency metrology, and the importance of this technology has been witnessed by a Nobel Prize in 2005 [23,24]. The recently developed QCL comb exhibits great potential with a high-power and broadband spectrum [25–30]. The high temporal resolution property

of the QCL comb has been exploited in kinetics research, such as the hydrolysis of guanosine triphosphate and the pyrolysis of iso-octane, covering biophysics and combustion diagnostics [31,32]. High-resolution molecular spectroscopy was achieved by employing a free-running dual QCL comb system with a MHz-level accurate frequency axis calibrated by current tuning procedures such as rapid-sweep mode and step-sweep mode [33,34]. Although significant advancements have been made, most of the demonstrated mid-IR QCL combs are concentrated at $\lambda \sim 7\text{--}9\ \mu\text{m}$ due to the naturally low GVDs of the QCL materials. The advantage of this spectral range is that it is easy to engineer a negative material dispersion by using a heavily doped plasma-enhanced waveguide to compensate the positive active region and waveguide dispersions, as has been done for QCL combs at $\lambda \sim 7\text{--}8\ \mu\text{m}$ [27–30]. However, for a QCL wavelength shorter than $6\ \mu\text{m}$, the dispersion engineering becomes challenging. The narrow bandgap material compositions such as InGaAs inside QCL induce large amounts of dispersion. This makes the self-starting frequency comb operation quite challenging.

We used a Gires–Tournois interferometer (GTI) mirror based on $\text{Y}_2\text{O}_3/\text{TiO}_2$ with an optimized waveguide design for shortwave QCL dispersion compensation. The QCL structure is based on a dual-stack active region structure with strain-balanced emitter designs at $\lambda \sim 4.5$ and $5.5\ \mu\text{m}$, which helps to increase the lasing spectral bandwidth and decrease the gain-induced dispersion [35]. The gain-induced dispersion in this work is estimated to be around $150\ \text{fs}^2/\text{mm}$, which is compared to $350\ \text{fs}^2/\text{mm}$ in Ref. [30]. A narrow intermode beating linewidth of $500\ \text{Hz}$ with a broad lasing spectral coverage of $100\ \text{cm}^{-1}$ and watt-level output power is observed at $\lambda \sim 5.0\ \mu\text{m}$. The multiheterodyne spectrum from the beating of two of these QCL combs exhibits 95 comb lines, which corresponds to an overlapping spectral range of $30\ \text{cm}^{-1}$, as shown in Figure 3 [35].

The thick GTI mirror coating would somehow affect the device's yield due to dielectric strain under a high optical power density. On the other hand, many enabling technologies such as high-speed optical transceivers and chip-scale photonic sensors have benefited from effective mid-infrared active–passive optical coupling. Recently, a high-power efficiency QCL comb based on a monolithic integrated multimode waveguide (MIMWG) design was reported, which achieves dispersion compensation based on the strong coupling between a single-mode active region and a multimode InGaAs-based passive WG [36]. Compared to the dispersion of a single-waveguide laser with the same core, the GVD is reduced by $\sim 1400\ \text{fs}^2/\text{mm}$ at a frequency of $2220\ \text{cm}^{-1}$, which illustrates the effectiveness of the MIMWG dispersion engineering design. The coherence information of the comb spectrum is measured by dual-comb multiheterodyne, two beams entering, respectively, the high-bandwidth MCT detector (Vigo UHSM-10.6 2.5 GHz cutoff frequency) to acquire the multiheterodyne signal and the spectrometer to measure the spectrum after being combined and split by the beam splitter. The linewidths of beat notes for the two combs are both less than $1\ \text{kHz}$, and the repetition frequency difference is tuned to $20\ \text{MHz}$. In addition, the dual-comb multiheterodyne spectra of the two combs are shown to cover about $1.2\ \text{GHz}$ and contain a total of about 50 combs with a repetition frequency of $20\ \text{MHz}$. The dual-comb tooth at $\sim 745\ \text{MHz}$ exhibits a FWHM of $0.63\ \text{MHz}$. This monolithic dispersion-engineered waveguide design is compatible with effective primary-passive optical coupling schemes and opens up new opportunities for mid-infrared photonic integrated circuits.

Rapid development has been reported for QCL combs in the terahertz (THz) range [37–42]; however, cryogenic cooling is still the precondition. Recently, we overcame this issue and reported a room temperature THz frequency comb at $3.0\ \text{THz}$ based on DFG from a mid-IR QCL comb [43]. A largely detuned distributed-feedback (DFB) grating (by $\sim 80\text{--}90\ \text{cm}^{-1}$ away from the gain peak) is integrated into the QCL cavity to provide the single-mode operation, as well as enhanced spatial hole burning effect for

the multimode comb operation, as shown in Figure 4a. Meanwhile, the grating coupling strength (κL , L = grating length) is set to be 3–5 to secure the single-mode operation. In the comb operating spectral range of 1240–1280 cm^{-1} , the calculated DFB dispersion is limited to $\pm 1500 \text{ fs}^2$, which is also verified by the dispersion testing results [43].

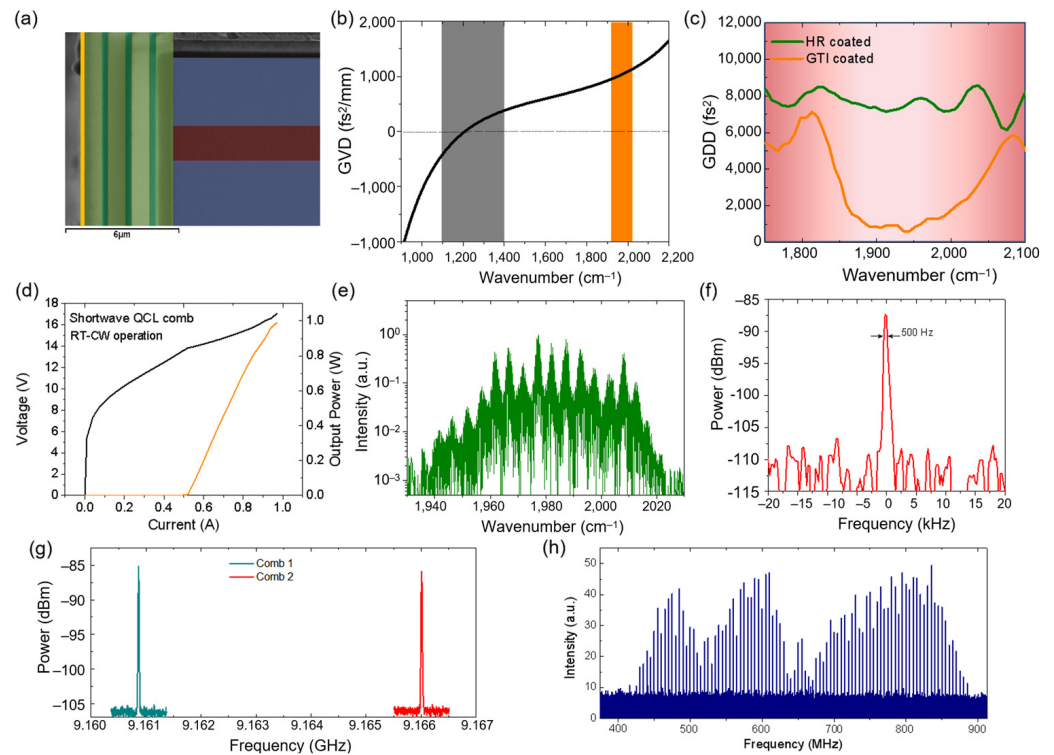


Figure 3. (a) SEM image of the cross-section of a typical GTI mirror coated on a QCL comb back facet for GVD engineering. The GTI, active region, InP cladding, and metal coatings are false-colored as light green, light red, light blue, and orange, respectively. (b) Calculated GVD for a typical QCL waveguide as a function of frequency. Gray-shaded area indicates the actively investigated spectral range of 7–9 μm , and the orange-shaded area indicates a high GVD at 5 μm . (c) Measured group delay dispersions of a high-reflection-coated device and a GTI-coated device. (d) P-I-V characterization of 5-mm-long, GTI-coated QCL comb devices in CW operation at 293 K. (e) Lasing spectrum in the logarithmic scale at 820 mA for the GTI-coated QCL device. (f) Electrical beat note spectrum at 820 mA. (g) Electrical beat note spectra of two QCL combs used for the multiheterodyne experiment. (h) Multiheterodyne beating of the two combs, corresponding to an optical bandwidth of 30 cm^{-1} . Adapted from Ref. [35].

The device emits a single mode at $\lambda_1 = 7.25 \mu\text{m}$, defined by the DFB grating period and a pronounced multimode emission at $\lambda_2 = 7.81 \mu\text{m}$ simultaneously, as shown in Figure 4b. Instead of an emitting dense state fundamental comb as the FP device, the detuned DFB device produces stable multimode emissions with a mode spacing corresponding to 14 times the free spectral range (FSR) of the laser cavity for currents $I \leq 1.5 \text{ A}$ and 22 times the FSR at higher currents. Thanks to the mid-IR harmonic state comb operation with a limited mode number, the converted THz comb state is concentrated on a limited number of comb modes with a side mode suppression ratio up to 20 dB (Figure 4e). The continuous THz power up to 5 μW was measured with a calibrated Golay cell detector. Multiheterodyne spectroscopy with multiple equally spaced lines by beating it with a reference Fabry–Pérot comb confirms the THz comb operation (Figure 4c,d). This type of THz comb provides a new solution to chip-based high-speed high-resolution THz spectroscopy with a compact size at room temperature.

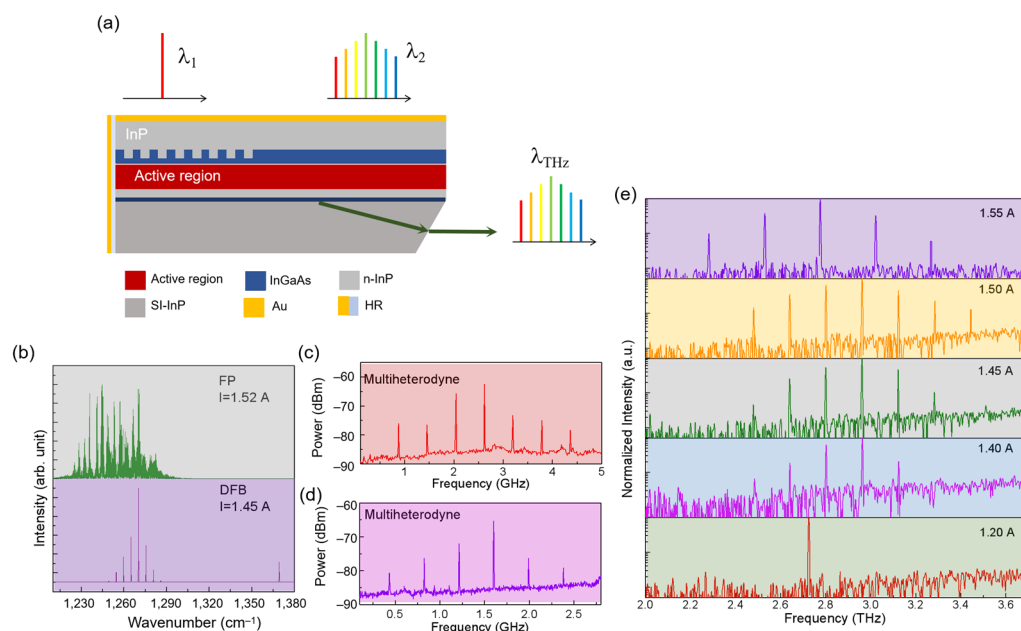


Figure 4. (a) Schematic of a largely detuned DFB design for a THz frequency comb based on QCL. (b) Multiheterodyne characterizations based on the DFB and FP QCL combs. Lasing spectrum of the FP comb at 1.52 A and the DFB comb at 1.45 A recorded with the FTIR, respectively. Multiheterodyne beating of the FP comb at 1.52 A and the DFB comb at 1.45 A (c) and the DFB comb at 1.55 A (d). (e) Lasing THz spectra of the DFB QCL comb evolving at different currents from 1.20 to 1.55 A at room temperature continuous wave operation. Adapted from Ref. [43].

3. Difference Frequency Generation THz QCL

Beginning with the exploration of terahertz electronics and terahertz time domain spectroscopy in the 1980s, research in the field of terahertz has rapidly expanded from basic science to real-world applications [44–46]. Due to the inability of THz QCLs to operate at room temperature and the bulky gas laser system, which limits their practical applications, nonlinear differential frequency effects have been introduced into terahertz quantum cascade lasers in order to realize on-chip room temperature terahertz light sources, and this principle is illustrated in Figure 5a.

The THz DFG QCL work was initiated in 2007 working at 80 K with a peak power of 60 nW [47]. In 2011, we introduce a composite grating to purifying the mid-IR pumping and thus single-mode operation for THz and achieved single-mode 4 THz radiated light emission with a room temperature peak power of 8.5 μ W [48]. Then, we demonstrated the DFG THz-QCL with a broad spectral coverage of 1–4.6 THz based on a Čerenkov phase matching scheme [49,50] and RT-cw power of 14 μ W at 3.4 THz [17,51], as shown in Figure 5e. In 2015, Razeghi’s group realized the world’s first THz surface emission could be achieved by designing a diffraction grating structure at the backside of the semi-insulating InP substrate, so as to collect THz light within the cavity length to satisfy the phase match condition, THz surface emission with a peak power of 0.5 mW at room temperature [52,53]. Subsequently, a Float zone high-resistivity (FZ HR) Si substrate was used to replace the semi-insulating InP substrate to enhance the THz outcoupling efficiency [54,55]. However, wafer bonding has been used, which limits the mass production of devices. Recently, Razeghi’s group reported the high-power high operating temperature of LW QCL directly on a Si substrate, which opens up the possibility of high-power, CW, RT operations of THz laser diodes and frequency combs in the near future for many different applications, especially free space optical communication [56,57]. With the gradual improvement and enhancement of the theoretical mechanism of DFG THz-QCL and the device performance,

a commercialized light source below 1 THz based on DFG THz-QCL for pharmaceutical imaging and drug analysis was introduced [58–61].

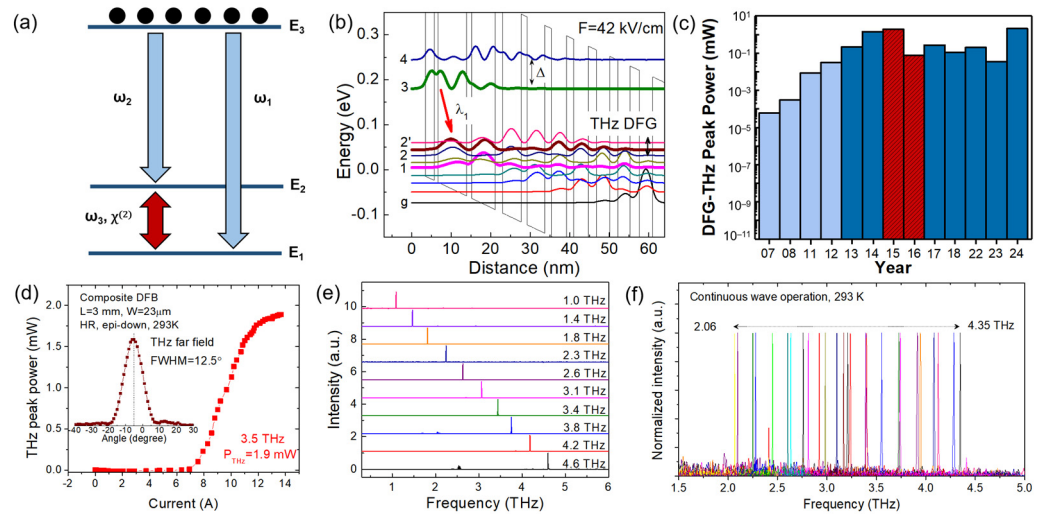


Figure 5. (a) Schematic descriptions of major DFG processes. (b) Conduction band and wave function diagram for the SPR design. (c) The trends of peak power for intracavity DFG-THz QCL. The light blue bars represent DFG-THz QCLs based on modal phase-matching scheme, the dark blue bars represent DFG-THz QCLs based on Čerenkov phase-matching scheme, the red bars represent DFG-THz QCLs with highest pulsed and CW powers from Refs. [10,17], respectively. (d) THz power characterization of DFG-THz QCL. The inset is the far-field distribution. (e) The THz spectra of the devices emitting from 1.0 to 4.6 THz. (f) Characterization of THz spectral tuning for the SGDFB-DBR devices designed with different frequency spacings. Adapted from Refs. [10,17,48,50].

The output power of the intracavity DFG THz-QCL mainly depends on the mid-infrared power W_{f1} and W_{f2} , the nonlinear coefficient $\chi^{(2)}$, the coherence length l_{coh} of the mid-infrared and terahertz waves, and the mode overlap coefficient S_{eff} , and the formula for each item is as follows [20,21]:

$$W_{f, THz} = \frac{\omega^2}{8\epsilon_0 c^3 n_1 n_2 n_{THz}} |\chi^{(2)}|^2 \times \frac{W_{f,1} W_{f,2}}{S_{eff}} \times l_{coh}^2 \quad (4)$$

where k_1 and k_2 are the propagation constants of the two mid-infrared pumps, z is the dipole moment array element, and Γ is the linewidth spreading factor, which is typically 10–15 meV in the mid-infrared band and 3–5 meV in the THz band.

Optimization in terms of the coherence length l_{coh} was performed, on the one hand, by replacing the n-InP substrate with a semi-insulating InP substrate to satisfy the Čerenkov phase-matching mode, which improves the coherence length to the order of the cavity length. On the other hand, the substrate is angle-polished to increase the outgoing efficiency of THz radiated waves.

At present, we are continuing the efforts on the power enhancement of THz DFG QCLs and just demonstrated the highest power record of 2.1 mW at RT recently, as shown in Figure 5c. All these this information concludes that, for the DFG THz-QCL power enhancement from a single laser chip, the increase of the optical power of the mid-infrared QCL is the next key step while maintaining others like nonlinear coefficient and coherence length in the optimal conditions.

4. Future of DFG THz QCL

While significant development has been made for THz DFG QCLs, a much higher THz power is highly desired to expand its application, since THz DFG QCL power is directly

proportional to the squared power of the pumping mid-IR QCL power. The mid-IR power upscaling with high beam quality and single-mode operation is the next important step in the development of DFG THz QCLs. The increase in WPE is important for reducing excessive heat and therefore increasing CW power, but achieving significantly higher output power can also simply be achieved by increasing the volume of the laser active region if the same WPE is maintained. However, power scaling of QCLs in CW mode is much more challenging than that in pulsed mode due to the significant heat in CW operations. Recently, CW power scaling of QCLs was successfully demonstrated in our group by using an array of narrow ridge optical phased-array (OPA) QCLs with a large enough pitch size for effective heat removal [19,62] (Figure 6a–c). A multimode interferometer (MMI) waveguide is designed for effective mode splitting and amplifying of the fundamental mode (Mode 0), and all the higher order modes (Modes 1, 2, 3, . . .) are filtered out, as shown in Figure 6b. A maximum CW power of 8.2 W is achieved at $I = 7.2$ A, which is limited by thermal rollover. The maximum WPE in CW mode is as high as 9.5% nominal and 10.1% after serial voltage correction.

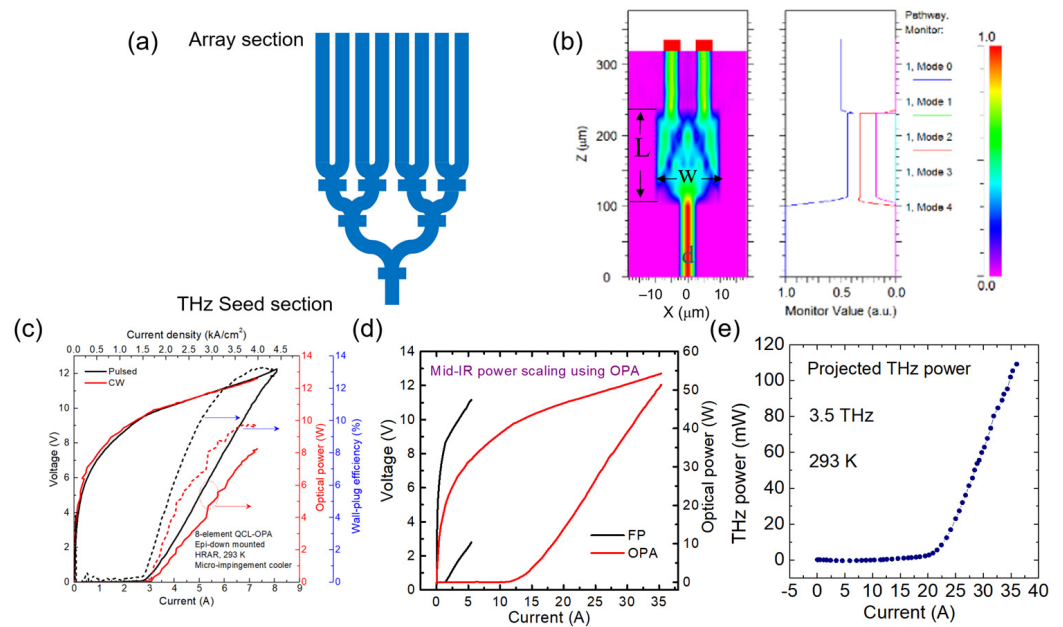


Figure 6. (a) Schematic of QCL optical phased array. (b) Mode propagation inside a MMI waveguide design simulated using the beam propagation method. (c) P-I-V and WPE characterization of an 8-element QCL OPA as functions of the current in a continuous wave operation. (d) P-I-V and WPE characterizations of a 16-element QCL OPA and a FP reference device as functions of the current in a pulsed mode operation. (e) Projected THz power of a THz DFG QCL using an OPA design. Figure (c) is adapted from Ref. [19].

In pulsed mode operation, the mid-IR can be readily upscaled to 50 W by using a 16-element OPA design, as shown in Figure 6d. With this kind of power level and a similar mid-IR-to-THz conversion efficiency, a projected THz power of over 100 mW is estimated, as shown in Figure 6e. This projected power would suffice for the THz power level required in many applications.

Although semi-insulating InP is much more transparent for THz waves than the n-type substrate, it still exhibits loss compared to the semi-insulating Si substrate and absorbs a great portion of the THz signal. Therefore, direct integration of a THz DFG QCL on a semi-insulating Si substrate would be an interesting approach for THz power enhancement. A more straightforward solution is the direct epitaxial growth of QCLs on the desired photonics platform like Si. Despite the 4–8% lattice constant mismatch to Si,

InP-based QCLs directly grown on Si have been gaining fast development over the past few years. Recently, our initial work on growing an InP-based QCL directly on a GaAs substrate was successful, with >14 W of peak power at room temperature [63]. While GaAs has only half the lattice mismatch to InP compared to Si, the results did provide hope that high-power Si-based QCLs could be achieved. A suitable template for the growth of InP-based devices on Si was first presented, grown entirely by MOCVD. A long wavelength QCL active region was then grown on this template using GSMBE and processed into a buried heterostructure laser for a proof-of-concept demonstration of high-power operation at room temperature [64]. Peak power up to 2.5 W is demonstrated, with a Jth as low as 1.3 kA/cm² and a slope efficiency up to 1.6 W/A. While the peak output power is similar, the demonstrated Si-based QCL exhibits a much lower threshold current density by a factor of 3.3 and a much higher wall plug efficiency by a factor of 3.67, both of which are critical for continuous operation.

This initial work provides proof-of-concept for the realization of longwave IR Si-based QCL capable of RT operation and high-power output for the first time. Early stage InP-on-GaAs templates were grown by MOCVD. The InP-on-Si templates were grown by GSMBE. The layer sequence and contact geometry exhibit relatively low series resistance and optical losses, though some optimization can still be done at this long wavelength [65]. Since this technology is based on InP, this approach is also directly transferred to near-infrared photonic integrated circuit (PIC) technology. It is reasonable to envision a single Si-based PIC which, with some creative active and waveguide designs, can be truly multispectral, covering from visible light to THz.

Finally, the THz DFG power actively benefits from the improvement of the WPE of the mid-IR pumping QCLs. The WPE of a QCL is the energy conversion efficiency from the electrical power input to the optical power output. Optimizing the WPE can not only efficiently take advantage of electrical energy but can also minimize the waste heat produced by a laser, which can significantly improve the reliability, especially for QCLs under cw operation. Unlike traditional quantum well semiconductor lasers with WPE capable of exceeding ~70% at RT [66], QCL requires a minimum voltage (typically above 10 V) to align the cascade structures before any gain behavior, which posts a challenge to improving the WPE. In addition, a lower quantum efficiency and stronger carrier thermalization during electron transport in minibands also prevent the increase of QCL WPE. In 2011, we reported a high-performance QCL with ~21% WPE in cw operation, and ~27% WPE in pulsed operation was demonstrated at room temperature [18]. This laser, based on the shallow well design with AlAs inserts in the barriers [67], consists of 40 QCL stages and is featured by a high characteristic temperature at $T_0 \approx 240$ K. Since then, no significant improvement of the cw WPE of QCLs has been reported. Although a newly designed QCL with ~28% pulsed WPE was demonstrated later but with a reduced characteristic temperature of $T_0 \approx 140$ K [68].

Figure 7a depicts a typical quantum band structure of a high efficiency QCL based on a strain-balanced InGaAs/InAlAs/InP material system. A large energy spacing between higher lasing levels E_3 and E_4 to suppress carrier leakage into the continuum and a single phonon resonance depopulation scheme for the lower levels are designed for high quantum efficiency. This has been the normal practice for high-efficiency QCL design. In fact, aside from further optimizing the quantum design of a QCL, its WPE can also be improved simply by increasing the thickness of the laser core (proportional to the number of QCL stages, N_s), as it can raise the waveguide optical confinement factor (Γ), reduce the waveguide

loss (α_w), and lower the threshold current density (J_{th}). A lower waveguide loss permits increasing the WPE (η_{wpe}) by lifting the optical efficiency (η_o), since [12]

$$\eta_{WPE} = \eta_i \frac{\alpha_m}{\alpha_m + \alpha_w} \frac{1}{1 + \Delta_{inj}/(\hbar\omega)} \left[1 - \frac{n_{trans}}{e_0 n_s} J_{th} \right] \quad (5)$$

$$\eta_i = \frac{\tau_{32} - \tau_2}{\tau_{32} + \tau_{32}\tau_2/\tau_3 - \tau_2} \quad (6)$$

$$J_{th} = \frac{e_0}{\tau_3(1 - \tau_2/\tau_{32})} \left(\frac{\alpha_m + \alpha_w}{N_s g_c} + n_s e^{-\Delta_{inj}/k_B T} \right) \quad (7)$$

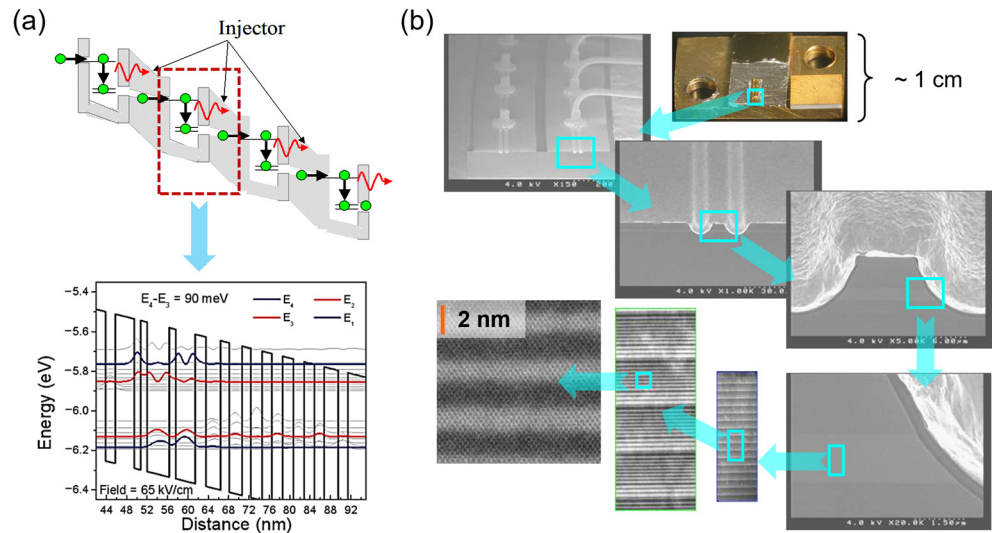


Figure 7. (a) Typical quantum band structure of QCL featuring a large energy spacing between the higher lasing levels and a single phonon resonance depopulation scheme for the lower levels. (b) Typical images of the scanning electron microscope (SEM) of QCL under different magnifications.

Here, $\eta_o = \alpha_m / (\alpha_m + \alpha_w)$, where η_i , η_v , η_e , and α_m are the internal quantum efficiency, voltage efficiency, electrical efficiency, and mirror loss, respectively [12]. A higher confinement factor enables WPE improvement by decreasing the threshold current density, because less gain (g) is required for lasing ($g = (\alpha_m + \alpha_w) / \Gamma$). However, increasing the N_s will also increase the temperature of the laser core in the cw operation, which will strongly degrade the performance. Thus, to achieve a higher cw WPE, a tradeoff between the active region confinement factor and thermal resistivity is required.

On the other hand, the high-quality, strain-balanced InGaAs/InAlAs material system is the key to high-power QCLs. Figure 7b shows the scanning electron microscope (SEM) images of the QCL under different magnifications. The judicious control of epitaxy over the layer thickness and the striking clear layer interface are the most important factors for high-quality QCL material growth.

The buried ridge regrowth process has been widely used in the fabrication of high-power cw QCLs [69,70]. After defining a laser ridge waveguide by wet etching two channels (~10 μm deep) on either side, the regrowth of semi-insulating Fe:InP cladding is performed by MOCVD to fill the channels. Figure 7b shows the scanning electron microscope (SEM) image of a typical buried ridge waveguide QCL under different magnifications. The buried ridge waveguide design will significantly reduce the optical loss and increase the thermal conductivity.

The low voltage efficiency η_v (<50%) is the primary reason for the lower wall plug efficiency compared to traditional semiconductor lasers with a voltage efficiency η_v close to 100%. However, this would not be an issue under cryogenic conditions when the thermal

backfilling is negligible. As such, the injector depth can be significantly reduced by using a one-well injector design [71]. A high wall plug efficiency of 53% is achieved from a one-well injector QCL at 40 K, which still holds the efficiency record up to now.

For room temperature operation, we set the injector depth at ~ 150 meV for QCL at $4.9 \mu\text{m}$, which is the current state-of-the-art design presented in Ref. [18]. By increasing the QCL stages from 40 to 45 and improving the quality of epitaxy processing, we demonstrate a QCL, emitting at $\sim 4.9 \mu\text{m}$ with the highest RT-cw WPE to date (22%), delivering 5.6 W optical power in a cw operation from a single facet [72]. A high optical power density of $\sim 35 \text{ MW}/\text{cm}^2$ was achieved at room temperature without damaging the outcoupling facet. This result represents an important milestone in CW QCL efficiency and output power and also illustrates the reproducibility of material growth and device fabrication quality in CQD/NU. Then, we further increase the cascade stage number to 50 and achieve a wall plug efficiency of $\sim 31\%$ and an output power of ~ 23 W in pulsed operations at room temperature [73].

The above steady improvements of the mid-IR pumping QCLs in the past few years will shed light on the enhancement of the THz DFG QCL power and conversion efficiency. Recently, high-performance QCLs grown by MOCVD have been demonstrated [74,75]. This is important to THz DFG QCL large-scale production and commercialization, since MOCVD technology is famous for its high-volume and low-cost production [3].

5. Conclusions and Perspectives

The QCL is becoming the leading semiconductor laser source in the mid-IR and THz frequency ranges thanks to the tremendous development in the past three decades. Particularly, the recent breakthroughs in high-power, high-efficiency QCLs, frequency combs based on QCLs, silicon-based QCLs, and room temperature intracavity DFG-THz QCLs are pushing QCL technology to new frontiers of research. Looking forward at the next decade, the major challenges facing THz DFG QCLs and frequency combs can be simply put: higher output power beyond the mW level for THz DFG QCL and high precision application using the QCL frequency comb. Both of these would benefit from elevating the WPE of QCL up to 50%. With further development of this technology, many new QCL-based applications in spectroscopy, sensing, and communication are likely to emerge in the near future.

Author Contributions: Writing—original draft preparation, Q.L.; writing—review and editing, M.R. and Q.L.; funding acquisition—M.R. All authors have read and agreed to the published version of the manuscript.

Funding: This work was supported by the National Science Foundation (Grant No. ECCS-2149908).

Acknowledgments: Authors would like to acknowledge the support of Walter P. Murphy Society.

Conflicts of Interest: The authors declare no conflict of interest.

References

1. Esaki, L.; Tsu, R. Superlattice and Negative Differential Conductivity in Semiconductors. *IBM J. Res. Dev.* **1970**, *14*, 61–65. [[CrossRef](#)]
2. Cho, A.Y.; Arthur, J.R. Molecular beam epitaxy. *Prog. Solid State Chem.* **1975**, *10*, 157–192. [[CrossRef](#)]
3. Razeghi, M. *The MOCVD Challenge: A Survey of GaInAsP-InP and GaInAsP-GaAs for Photonic and Electronic Device Applications*, 2nd ed.; CRC Press: Boca Raton, FL, USA, 2010; pp. 1–773.
4. Kazarinov, R.F.; Suris, R.A. Possibility of amplification of electromagnetic waves in a semiconductor with a superlattice. *Sov. Phys.* **1970**, *5*, 707–709.
5. Faist, J.; Capasso, F.; Sivco, D.L.; Sirtori, C.; Hutchinson, A.L.; Cho, A.Y. Quantum cascade laser. *Science* **1994**, *264*, 553–556. [[CrossRef](#)]

6. Razeghi, M. A lifetime of contributions to the world of semiconductors using the Czochralski invention. *J. Vacuum* **2017**, *146*, 308. [[CrossRef](#)]
7. Slivken, S.; Jelen, C.; Rybaltowski, A.; Diaz, J.; Razeghi, M. Gas-source molecular beam epitaxy growth of an 8.5 μm quantum cascade laser. *Appl. Phys. Lett.* **1997**, *71*, 2593–2595. [[CrossRef](#)]
8. Yao, Y.; Hoffman, A.J.; Gmachl, C.F. Mid-infrared quantum cascade lasers. *Nat. Photonics* **2012**, *6*, 432–439. [[CrossRef](#)]
9. Vitiello, M.S.; Scalari, G.; Williams, B.; De Natale, P. Quantum cascade lasers: 20 years of challenges. *Opt. Express* **2015**, *23*, 5167–5182. [[CrossRef](#)]
10. Razeghi, M.; Lu, Q.Y.; Bandyopadhyay, N.; Zhou, W.; Heydari, D.; Bai, Y.; Slivken, S. Quantum cascade lasers: From tool to product. *Opt. Express* **2015**, *23*, 8462–8475. [[CrossRef](#)]
11. Curl, R.F.; Capasso, F.; Gmachl, C.; Kosterev, A.A.; McManus, B.; Lewicki, R.; Pusharsky, M.; Wysocki, G.; Tittel, F.K. Quantum cascade lasers in chemical physics. *Chem. Phys. Lett.* **2010**, *487*, 1–18. [[CrossRef](#)]
12. Razeghi, M. High-Performance InP-Based Mid-IR Quantum Cascade Lasers. *IEEE J. Sel. Top. Quant.* **2009**, *15*, 941–951. [[CrossRef](#)]
13. Faist, J. *Quantum Cascade Lasers*; Oxford University Press: Oxford, UK, 2013.
14. Razeghi, M.; Zhou, W.J.; Slivken, S.; Lu, Q.Y.; Wu, D.H.; McClintock, R. Recent progress of quantum cascade laser research from 3 to 12 μm at the Center for Quantum Devices [Invited]. *Appl. Opt.* **2017**, *56*, H30–H44. [[CrossRef](#)] [[PubMed](#)]
15. Botez, D.; Belkin, M.A. *Mid-Infrared and Terahertz Quantum Cascade Lasers*; Cambridge University Press: Cambridge, UK, 2023.
16. Bandyopadhyay, N.; Bai, Y.; Tsao, S.; Nida, S.; Slivken, S.; Razeghi, M. Room temperature continuous wave operation of lambda similar to 3-3.2 μm quantum cascade lasers. *Appl. Phys. Lett.* **2012**, *101*, 241110. [[CrossRef](#)]
17. Lu, Q.Y.; Wu, D.H.; Sengupta, S.; Slivken, S.; Razeghi, M. Room temperature continuous wave, monolithic tunable THz sources based on highly efficient mid-infrared quantum cascade lasers. *Sci. Rep.* **2016**, *6*, 23595. [[CrossRef](#)] [[PubMed](#)]
18. Bai, Y.; Bandyopadhyay, N.; Tsao, S.; Slivken, S.; Razeghi, M. Room temperature quantum cascade lasers with 27% wall plug efficiency. *Appl. Phys. Lett.* **2011**, *98*, 181102. [[CrossRef](#)]
19. Zhou, W.J.; Lu, Q.Y.; Wu, D.H.; Slivken, S.; Razeghi, M. High-power, continuous-wave, phase-locked quantum cascade laser arrays emitting at 8 μm . *Opt. Express* **2019**, *27*, 15776–15785. [[CrossRef](#)] [[PubMed](#)]
20. Shen, Y.R. *The Principles of Nonlinear Optics*; Wiley: New York, NY, USA, 1984.
21. Belkin, M.A.; Capasso, F.; Xie, F.; Belyanin, A.; Fischer, M.; Wittmann, A.; Faist, J. Room temperature terahertz quantum cascade laser source based on intracavity difference-frequency generation. *Appl. Phys. Lett.* **2008**, *92*, 201101. [[CrossRef](#)]
22. Friedli, P.; Sigg, H.; Hinkov, B.; Hugi, A.; Riedi, S.; Beck, M.; Faist, J. Four-wave mixing in a quantum cascade laser amplifier. *Appl. Phys. Lett.* **2013**, *102*, 222104. [[CrossRef](#)]
23. Udem, T.; Holzwarth, R.; Hänsch, T.W. Optical frequency metrology. *Nature* **2002**, *416*, 233–237. [[CrossRef](#)] [[PubMed](#)]
24. The Nobel Prize in Physics 2005. Available online: <https://www.nobelprize.org/prizes/physics/2005/9807-the-nobel-prize-in-physics-2005-2005-6/> (accessed on 1 November 2024).
25. Hugi, A.; Villares, G.; Blaser, S.; Liu, H.C.; Faist, J. Mid-infrared frequency comb based on a quantum cascade laser. *Nature* **2012**, *492*, 229. [[CrossRef](#)]
26. Lu, Q.Y.; Razeghi, M.; Slivken, S.; Bandyopadhyay, N.; Bai, Y.; Zhou, W.J.; Chen, M.; Heydari, D.; Haddadi, A.; McClintock, R.; et al. High power frequency comb based on mid-infrared quantum cascade laser at $\lambda \sim 9 \mu\text{m}$. *Appl. Phys. Lett.* **2015**, *106*, 051105. [[CrossRef](#)]
27. Villares, G.; Riedi, S.; Wolf, J.; Kazakov, D.; Süess, M.; Faist, J. Dispersion engineering of quantum cascade laser frequency combs. *Optica* **2016**, *3*, 252–258. [[CrossRef](#)]
28. Lu, Q.Y.; Wu, D.H.; Slivken, S.; Razeghi, M. High efficiency quantum cascade laser frequency comb. *Sci. Rep.* **2017**, *7*, 43806. [[CrossRef](#)]
29. Yves, B.; Ilia, S.; Wolf, W.; Richard, M.; Tobias, G.; Alfredo, B.; Stéphane, B.; Antoine, M.; Faist, J. Plasmon-enhanced waveguide for dispersion compensation in mid-infrared quantum cascade laser frequency combs. *Opt. Lett.* **2017**, *42*, 1604–1607.
30. Lu, Q.Y.; Manna, S.; Slivken, S.; Wu, D.H.; Razeghi, M. Dispersion compensated mid-infrared quantum cascade laser frequency comb with high power output. *AIP Adv.* **2017**, *7*, 045313. [[CrossRef](#)]
31. Norahan, M.J.; Horvath, R.; Woitzik, N.; Jouy, P.; Eigenmann, F.; Gerwert, K.; Köttling, C. Microsecond-Resolved Infrared Spectroscopy on Nonrepetitive Protein Reactions by Applying Caged Compounds and Quantum Cascade Laser Frequency Combs. *Anal. Chem.* **2021**, *93*, 6779–6783. [[CrossRef](#)] [[PubMed](#)]
32. Pinkowski, N.H.; Cassady, S.J.; Strand, C.L.; Hanson, R.K. Quantum-cascade-laser-based dual-comb thermometry and speciation at high temperatures. *Meas. Sci. Technol.* **2021**, *32*, 035501. [[CrossRef](#)]
33. Gianella, M.; Nataraj, A.; Tuzson, B.; Jouy, P.; Kapsalidis, F.; Beck, M.; Mangold, M.; Hugi, A.; Faist, J.; Emmenegger, L. High-resolution and gapless dual comb spectroscopy with current-tuned quantum cascade lasers. *Opt. Express* **2020**, *28*, 6197–6208. [[CrossRef](#)] [[PubMed](#)]

34. Lepère, M.; Browet, O.; Clément, J.; Vispoel, B.; Allmendinger, P.; Hayden, J.; Eigenmann, F.; Hugli, A.; Mangold, M. A mid-infrared dual-comb spectrometer in step-sweep mode for high-resolution molecular spectroscopy. *J. Quant. Spectrosc. Radiat. Transf.* **2022**, *287*, 108239. [[CrossRef](#)]
35. Lu, Q.Y.; Manna, S.; Wu, D.H.; Slivken, S.; Razeghi, M. Shortwave quantum cascade laser frequency comb for multi-heterodyne spectroscopy. *Appl. Phys. Lett.* **2018**, *112*, 141104. [[CrossRef](#)]
36. Wu, D.P.; Ma, Y.; Sun, Y.Q.; Huang, R.X.; Zhang, J.C.; Liu, S.M.; Zhuo, N.; Zhai, S.Q.; Cheng, F.M.; Liu, F.Q.; et al. Monolithic Dispersion Engineered Mid-Infrared Quantum Cascade Laser Frequency Comb. *Photonics Res.* **2024**, *12*, 528787. [[CrossRef](#)]
37. Köhler, R.; Tredicucci, A.; Beltram, F.; Beere, H.E.; Linfield, E.H.; Davies, A.G.; Ritchie, D.A.; Iotti, R.C.; Rossi, F. Terahertz semiconductor-heterostructure laser. *Nature* **2002**, *417*, 156–159. [[CrossRef](#)]
38. Burghoff, D.; Kao, T.-Y.; Han, N.; Chan, C.W.I.; Cai, X.; Yang, Y.; Hayton, D.J.; Gao, J.-R.; Reno, J.L.; Hu, Q. Terahertz laser frequency combs. *Nat. Photon.* **2014**, *8*, 462–467. [[CrossRef](#)]
39. Rösch, M.; Scalari, G.; Beck, M.; Faist, J. Octave-spanning semiconductor laser. *Nat. Photonics* **2015**, *9*, 42–47. [[CrossRef](#)]
40. Consolino, L.; Nafa, M.; Cappelli, F.; Garrasi, K.; Mezzapesa, F.P.; Li, L.; Davies, A.G.; Linfield, E.H.; Vitiello, M.S.; De Natale, P.; et al. Fully phase-stabilized quantum cascade laser frequency comb. *Nat. Commun.* **2019**, *10*, 2938. [[CrossRef](#)] [[PubMed](#)]
41. Garrasi, K.; Mezzapesa, F.P.; Salemi, L.; Li, L.; Consolino, L.; Bartalini, S.; De Natale, P.; Davies, A.G.; Linfield, E.H.; Vitiello, M.S. High dynamic range, heterogeneous, terahertz quantum cascade lasers featuring thermally-tunable frequency comb operation over a broad current range. *ACS Photonics* **2019**, *6*, 73–78. [[CrossRef](#)]
42. Yang, Y.; Burghoff, D.; Hayton, D.J.; Gao, J.R.; Reno, J.L.; Hu, Q. Terahertz multi-heterodyne spectroscopy using laser frequency combs. *Optica* **2016**, *3*, 499–502. [[CrossRef](#)]
43. Lu, Q.Y.; Wang, F.; Wu, D.H.; Slivken, S.; Razeghi, M. Room temperature terahertz semiconductor frequency comb. *Nat. Commun.* **2019**, *10*, 2403. [[CrossRef](#)] [[PubMed](#)]
44. Ferguson, B.; Zhang, X.C. Materials for terahertz science and technology. *Na. Mater.* **2002**, *1*, 26–33. [[CrossRef](#)]
45. Siegel, P.H. Terahertz technology. *IEEE Trans. Microw. Theory Tech.* **2002**, *50*, 910–928. [[CrossRef](#)]
46. Tonouchi, M. Cutting-edge terahertz technology. *Nat. Photon.* **2007**, *1*, 97–105. [[CrossRef](#)]
47. Belkin, M.A.; Capasso, F.; Belyanin, A.; Sivco, D.L.; Cho, A.Y.; Oakley, D.C.; Vineis, C.J.; Turner, G.W. Terahertz quantum-cascade-laser source based on intracavity difference-frequency generation. *Nat. Photonics* **2007**, *1*, 288–292. [[CrossRef](#)]
48. Lu, Q.Y.; Bandyopadhyay, N.; Slivken, S.; Bai, Y.; Razeghi, M. Room temperature single-mode terahertz sources based on intracavity difference-frequency generation in quantum cascade lasers. *Appl. Phys. Lett.* **2011**, *99*, 131106. [[CrossRef](#)]
49. Vijayraghavan, K.; Adams, R.W.; Vizbaras, A.; Jang, M.; Grasse, C.; Boehm, G.; Amann, M.C.; Belkin, M.A. Terahertz sources based on Čerenkov difference-frequency generation in quantum cascade lasers. *Appl. Phys. Lett.* **2012**, *100*, 241104. [[CrossRef](#)]
50. Lu, Q.Y.; Bandyopadhyay, N.; Slivken, S.; Bai, Y.; Razeghi, M. Widely tuned room temperature terahertz quantum cascade laser sources based on difference-frequency generation. *Appl. Phys. Lett.* **2012**, *101*, 251121. [[CrossRef](#)]
51. Lu, Q.Y.; Bandyopadhyay, N.; Slivken, S.; Bai, Y.; Razeghi, M. Continuous operation of a monolithic semiconductor terahertz source at room temperature. *Appl. Phys. Lett.* **2014**, *104*, 221105. [[CrossRef](#)]
52. Razeghi, M.; Lu, Q.Y.; Bandyopadhyay, N.; Slivken, S. Recent development of high power, widely tunable THz quantum cascade laser sources based on difference-frequency generation. In *Unmanned/Unattended Sensors and Sensor Networks XI; and Advanced Free-Space Optical Communication Techniques and Applications*; SPIE Security + Defence: Bellingham, WA, USA, 2015; p. 9647.
53. Lu, Q.Y.; Razeghi, M. Recent Advances in Room Temperature, High-Power Terahertz Quantum Cascade Laser Sources Based on Difference-Frequency Generation. *Photonics* **2016**, *3*, 42. [[CrossRef](#)]
54. Jung, S.; Kim, J.H.; Jiang, Y.; Vijayraghavan, K.; Belkin, M.A. Terahertz difference-frequency quantum cascade laser sources on silicon. *Optica* **2017**, *4*, 38–43. [[CrossRef](#)]
55. Alyabyeva, L.N.; Zhukova, E.S.; Belkin, M.A.; Gorshunov, B.P. Dielectric properties of semi-insulating Fe-doped InP in the terahertz spectral region. *Sci. Rep.* **2017**, *7*, 7360. [[CrossRef](#)] [[PubMed](#)]
56. Johnson, S.M.; Dial, E.; Razeghi, M. High-speed free space optical communications based on quantum cascade lasers and type-II superlattice detectors. In *Quantum Sensing and Nano Electronics and Photonics XVII*; SPIE: Bellingham, WA, USA, 2020; Volume 11288, pp. 175–181.
57. Slivken, S.; Razeghi, M. High Power, Room Temperature InP-Based Quantum Cascade Laser Grown on Si. *IEEE J. Quantum Electron.* **2022**, *58*, 2300206. [[CrossRef](#)]
58. Fujita, K.; Hitaka, M.; Ito, A.; Edamura, T.; Yamanishi, M.; Jung, S.; Belkin, M.A. Terahertz generation in mid-infrared quantum cascade lasers with a dual-upper-state active region. *Appl. Phys. Lett.* **2015**, *106*, 251104. [[CrossRef](#)]
59. Nakanishi, A.; Fujita, K.; Horita, K.; Takahashi, H. Terahertz imaging with room-temperature terahertz difference-frequency quantum-cascade laser sources. *Opt. Express* **2019**, *27*, 1884–1893. [[CrossRef](#)] [[PubMed](#)]
60. Hayashi, S.; Ito, A.; Hitaka, M.; Fujita, K. Room temperature, single-mode 1.0 THz semiconductor source based on long-wavelength infrared quantum-cascade laser. *Appl. Phys. Express* **2020**, *13*, 112001. [[CrossRef](#)]

61. Fujita, K.; Hayashi, S.; Ito, A.; Dougakiuchi, T.; Hitaka, M.; Nakanishi, A. Broadly tunable lens-coupled nonlinear quantum cascade lasers in the sub-THz to THz frequency range. *Photonics Res.* **2022**, *10*, 703. [[CrossRef](#)]
62. Zhou, W.J.; Wu, D.H.; Lu, Q.Y.; Slivken, S.; Razeghi, M. Single-mode, high-power, mid-infrared, quantum cascade laser phased arrays. *Sci. Rep.* **2018**, *8*, 14866. [[CrossRef](#)] [[PubMed](#)]
63. Slivken, S.; Razeghi, M. High power mid-infrared quantum cascade lasers grown on GaAs. *Photonics* **2022**, *9*, 231. [[CrossRef](#)]
64. Slivken, S.; Razeghi, M. Room Temperature, Continuous Wave Quantum Cascade Laser Grown Directly on a Si Wafer. *IEEE Quantum Electron.* **2023**, *59*, 2300206. [[CrossRef](#)]
65. Cristobal, E.; Fetters, M.; Liu, A.W.; Fastenau, J.M.; Azim, A.; Milbocker, L.; Lyakh, A. High peak power quantum cascade lasers monolithically integrated onto silicon with high yield and good near-term reliability. *Appl. Phys. Lett.* **2023**, *122*, 141108. [[CrossRef](#)]
66. Knigge, A.; Erbert, G.; Jönsson, J.; Pittroff, W.; Staske, R.; Sumpf, B.; Weyers, M.; Trankle, G. Passively cooled 940 nm laser bars with 73% wall-plug efficiency at 70 W and 25 °C. *Electron. Lett.* **2005**, *41*, 250. [[CrossRef](#)]
67. Bai, Y.; Bandyopadhyay, N.; Tsao, S.; Selcuk, E.; Slivken, S.; Razeghi, M. Highly temperature insensitive quantum cascade lasers. *Appl. Phys. Lett.* **2010**, *97*, 251104. [[CrossRef](#)]
68. Lyakh, A.; Suttinger, M.; Go, R.; Figueiredo, P.; Todi, A. 5.6 μm quantum cascade lasers based on a two-material active region composition with a room temperature wall-plug efficiency exceeding 28%. *Appl. Phys. Lett.* **2016**, *109*, 121109. [[CrossRef](#)]
69. Beck, M.; Hofstetter, D.; Aellen, T.; Faist, J.; Oesterle, U.; Ilegems, M.; Gini, E.; Melchior, H. Continuous wave operation of a mid-infrared semiconductor laser at room temperature. *Science* **2002**, *295*, 301–305. [[CrossRef](#)] [[PubMed](#)]
70. Wang, F.; Slivken, S.; Wu, D.H.; Lu, Q.Y.; Razeghi, M. Continuous wave quantum cascade lasers with 5.6 W output power at room temperature and 41% wall-plug efficiency in cryogenic operation. *AIP Adv.* **2020**, *10*, 055120. [[CrossRef](#)]
71. Bai, Y.; Slivken, S.; Kuboya, S.; Darvish, S.R.; Razeghi, M. Quantum cascade lasers that emit more light than heat. *Nat. Photon.* **2010**, *4*, 99–102. [[CrossRef](#)]
72. Wang, F.; Slivken, S.; Wu, D.H.; Razeghi, M. Room temperature quantum cascade lasers with 22% wall plug efficiency in continuous-wave operation. *Opt. Express* **2020**, *28*, 17532. [[CrossRef](#)] [[PubMed](#)]
73. Wang, F.; Slivken, S.; Wu, D.H.; Razeghi, M. Room temperature quantum cascade laser with ~31% wall-plug efficiency. *AIP Adv.* **2020**, *10*, 075012. [[CrossRef](#)]
74. Botez, D.; Kirch, J.; Boyle, C.; Oresick, K.; Sigler, C.; Kim, H.; Knipfer, B.; Ryu, J.; Lindberg, D.; Earles, T.; et al. High-efficiency, high-power mid-infrared quantum cascade lasers [Invited]. *Opt. Mater. Express* **2018**, *8*, 1378–1398. [[CrossRef](#)]
75. Fei, T.; Zhai, S.Q.; Zhang, J.C.; Lu, Q.Y.; Zhuo, N.; Liu, J.Q.; Wang, L.J.; Liu, S.M.; Jia, Z.W.; Li, K.; et al. 3 W Continuous-Wave Room Temperature Quantum Cascade Laser Grown by Metal-Organic Chemical Vapor Deposition. *Photonics* **2023**, *10*, 47. [[CrossRef](#)]

Disclaimer/Publisher’s Note: The statements, opinions and data contained in all publications are solely those of the individual author(s) and contributor(s) and not of MDPI and/or the editor(s). MDPI and/or the editor(s) disclaim responsibility for any injury to people or property resulting from any ideas, methods, instructions or products referred to in the content.